HHS Public Access

Author manuscript

Biomaterials. Author manuscript; available in PMC 2023 January 01.

Published in final edited form as:

Biomaterials. 2022 January ; 280: 121318. doi:10.1016/j.biomaterials.2021.121318.

3D-Printed Oxygen-Releasing Scaffolds Improve Bone Regeneration in Mice

Ashley L. Farris[1,2], **Dennis Lambrechts**[1,2], **Yuxiao Zhou**[1,2], **Nicholas Y. Zhang**[1,2], **Naboneeta Sarkar**[1,2], **Megan C. Moorer**[3,4], **Alexandra N. Rindone**[1,2], **Ethan L. Nyberg**[1,2], **Alexander Perdomo-Pantoja**[5], **S. J. Burris**[1,2], **Kendall Free**[2,6], **Timothy F. Witham**[5], **Ryan C. Riddle**[3,4], **Warren L. Grayson**[*,1,2,6,7,8]

[1]Department of Biomedical Engineering, Johns Hopkins University School of Medicine, Baltimore, MD, USA

[2]Translational Tissue Engineering Center, Johns Hopkins University School of Medicine, Baltimore, MD, USA

[3]Department of Orthopedic Surgery, Johns Hopkins University School of Medicine, Baltimore, MD

[4]Baltimore Veterans Administration Medical Center, Baltimore, MD, USA

[5]Department of Neurosurgery, Johns Hopkins University School of Medicine, Baltimore, MD

[6]Department of Materials Science and Engineering, Johns Hopkins University, Baltimore, MD, USA

[7]Department of Chemical & Biomolecular Engineering, Johns Hopkins University, Baltimore, MD, USA

[8]Institute for NanoBioTechnology, Johns Hopkins University, Baltimore, MD

[*]Corresponding author: wgrayson@jhmi.edu.

Declaration of Competing Interest

The authors declare no conflict of interest.

The authors declare that they have no known competing financial interests or personal relationships that could have appeared to influence the work reported in this paper.

Data Availability Statement

The raw/processed data required to reproduce these findings cannot be shared at this time due to technical or time limitations. They can be made available upon request.

Credit Author Statement

Ashley Farris: Designed research, performed research, analyzed data, wrote the paper. Dennis Lambrechts: Designed research, performed research, analyzed data. Yuxiao Zhou: Performed research, analyzed data. Nicholas Zhang: Performed research, analyzed data. Naboneeta Sarkar: performed research, analyzed data, helped with revisions. Megan Moorer: Performed research, analyzed data. Alexandra Rindone: Performed research. Ethan Nyberg: Performed research. Alexander Perdomo-Pantoja: Performed research. S.J. Burris: Performed research. Kendall Free: Performed research. Ryan Riddle: Designed research, analyzed data. Warren Grayson: Designed research, analyzed data, wrote the paper.

Declaration of interests

The authors declare that they have no known competing financial interests or personal relationships that could have appeared to influence the work reported in this paper.

Abstract

Low oxygen (O_2) diffusion into large tissue engineered scaffolds hinders the therapeutic efficacy of transplanted cells. To overcome this, we previously studied hollow, hyperbarically-loaded microtanks (μtanks) to serve as O_2 reservoirs. To adapt these for bone regeneration, we fabricated biodegradable μtanks from polyvinyl alcohol and poly(lactic-co-glycolic acid) and embedded them to form 3D-printed, porous poly-ε-caprolactone (PCL)-μtank scaffolds. PCL-μtank scaffolds were loaded with pure O_2 at 300 – 500 psi. When placed at atmospheric pressures, the scaffolds released O_2 over a period of up to 8 hours. We confirmed the inhibitory effects of hypoxia on the osteogenic differentiation of human adipose-derived stem cells (hASCs and we validated that μtank-mediated transient hyperoxia had no toxic impacts on hASCs, possibly due to upregulation of endogenous antioxidant regulator genes. We assessed bone regeneration *in vivo* by implanting O_2-loaded, hASC-seeded, PCL-μtank scaffolds into murine calvarial defects (4 mm diameters × 0.6 mm height) and subcutaneously (4 mm diameter × 8 mm height). In both cases we observed increased deposition of extracellular matrix in the O_2 delivery group along with greater osteopontin coverages and higher mineral deposition. This study provides evidence that even short-term O_2 delivery from PCL-μtank scaffolds may enhance hASC-mediated bone tissue regeneration.

Keywords

osteogenesis; bone tissue engineering; oxygen delivery; 3D-printing; adipose-derived stem cells; microtanks

Introduction:

Tissue engineering approaches have been used to treat critically-sized, non-healing bone defects in pre-clinical models using a combination of biomaterials, cells, and biological factors[1–3]. Yet, there remains a critical period between the implantation of cellularized scaffolds and vascular infiltration into the defect in which cells are exposed to harsh, hypoxic environments. Consequently, maintaining cell function following implantation remains an obstacle in scaling up to clinically-relevant defect sizes due to prevailing ischemic microenvironments. Several strategies to overcome this limitation have been investigated, including the use of bioreactors to mature the tissues *in vitro* or *in vivo* prior to transplanting into the defect site[1,2,4], pre-vascularization of engineered grafts[5], hypoxic pre-conditioning to improve post-implantation cell survival rates that rely upon metabolic adaptations[6], and delivery of growth factors to induce rapid angiogenesis from adjacent host tissues[7,8]. One key strategy that has emerged is the transient co-delivery of oxygen (O_2) with the tissue engineered graft. This provides the cells with a more hospitable environment upon implantation, promotes their post-transplantation survival, and enhances their tissue regeneration capacity.

O_2 has important roles in both metabolism and signaling. In anaerobic environments, cells can maintain their ATP stores by relying upon glycolysis; however, oxidative phosphorylation produces 15 times more ATP per glucose molecule than glycolysis alone[9], resulting in rapid depletion in glucose stores when cells do not have access to a robust

vascular network. Furthermore, O_2 is necessary for a variety of important biological processes including protein synthesis, nucleic acid synthesis, and fatty acid desaturation. Prolonged periods of extreme hypoxia (<0.5% O_2), lead to cell necrosis because cells cannot maintain biomolecule production and ion gradients[10], which can have negative impacts on regeneration. In native tissues, oxygen typically is only capable of diffusing approximately 100–200μm away from native capillaries. Therefore, simple diffusion is insufficient to maintain viability of the transplanted metabolically active cells in large non-vascularized scaffolds > 1 mm. Due to the oxygen diffusion limitation, in a model of bone regeneration, mineralized tissue was only observed within a penetration depth of 200–300 μm from the scaffold edges[11,12]. Thus, groups have studied O_2 delivery to improve tissue engineering and tissue healing.

Previously, hyperbaric O_2 therapy has been shown to have benefits in bone regeneration in mice, rats, and rabbits[13–16]. This treatment involves placing a patient in a chamber where they are subjected to elevated O_2 concentrations and pressures for short periods of time. These studies applied repeated administration of hyperbaric O_2 therapy, with some regimens consisting of thirty 90-minute sessions over six weeks[15]. Extensive treatment would require patient compliance and could limit the clinical efficacy of this method to treat bone defects. Furthermore, hyperbaric oxygen therapy has been associated with rare, but severe side effects such as seizure and hypertension[17]. By providing O_2 locally within a tissue engineered construct, some of the negative systemic effects might be circumvented. Local O_2 delivery has been previously accomplished using peroxide, hemoglobin, and perfluorocarbon-based technologies to deliver O_2 to cells encapsulated within engineered scaffolds[17]. While these methods are promising, they suffer from various drawbacks: peroxides necessarily produce reactive O_2 species which can be harmful to cells[18], hemoglobin-based materials can induce reactive oxygen species production, vasoconstriction, and hypertension[19,20]. Perfluorocarbons contain cytotoxic emulsifying agents[21] and decrease the mechanical properties of scaffolds[22]. Additionally, perfluorocarbons and hemoglobin-based strategies are better suited to applications in engineering soft tissue rather than bone, as the former can reduce mechanical integrity of scaffolds and the latter are not stable in the harsher fabrication environments necessary for creating mechanically robust scaffolds. We previously investigated the fabrication of hollow microparticles that can be used to store O_2 following hyperbaric loading.

In earlier studies, hollow polyacrylonitrile microtanks (μtanks) were incorporated into poly-ε-caprolactone (PCL) discs and hyperbarically loaded with 100% O_2. The subsequent O_2 release when disks were placed in ambient atmospheric pressure in proximity to cultured cells improved cell viability in hypoxic conditions. However, polyacrylonitrile is not biodegradable. We therefore sought to fabricate μtanks from clinically used, biodegradable polymers, polyvinyl alcohol (PVA) and poly(lactic-co-glycolic acid) (PLGA). PVA is employed to form the ‘primary storage’ or inner shell of the μtank because of its low permeability to O_2, which allows it to control the oxygen release kinetics. However, PVA is susceptible to rapid hydrolytic degradation, which might result in the burst release of the O_2. To address this limitation, PLGA is utilized to coat PVA and form a secondary layer to increase durability and prevent early degradation of the μtank.

Incorporating O_2 delivery into 3D-printed scaffolds could enhance the utility of these biomaterials to regenerate craniofacial bone. 3D-printing scaffolds for tissue engineering has been widely investigated, as it allows for tight control of scaffold geometry and architecture. This feature has particular utility in the regeneration of craniofacial bone, as reproduction of native aesthetics are an important outcome of treatment[23]. Fused deposition modeling, the layer-by-layer deposition of a thermoplastic polymer into desired shapes, facilitates the incorporation of bioactive molecules such as decellularized bone or hydroxyapatite to improve osteogenesis[24]. The regenerative potential of the 3D-printed PCL-decellularized bone may be further enhanced by incorporating O_2 releasing μtanks which could enhance the viability of the transplanted stem cells.

In this study, we combined PVA-PLGA μtanks with PCL and 3D-printed the mixture into porous, PCL-μtank scaffolds. The PCL-μtank scaffolds were hyperbarically loaded with 100% O_2 and we seeded human adipose-derived stromal/stem cells (hASCs) into the pore spaces. We hypothesized that: (1) varying the concentration of μtanks in the scaffold and the O_2 loading pressure would allow us to tune the rate and amount of O_2 delivered to cells seeded into the pore spaces of the scaffolds, and (2) O_2 delivery from 3D-printed PCL-μtank scaffolds would improve regenerative outcomes in murine models of bone healing. Furthermore, uniform incorporation of μtanks into the struts of a 3D-printed scaffold would allow for future scale-up to larger grafts with application to a wide range of defect geometries[25]. To test these hypotheses we assessed manufacturability, characterized O_2-release kinetics, and investigated the effects of O_2 delivery on hASCs both *in vitro* and *in vivo*.

Results:

A graphical scheme of experiments has been provided as Supplementary Figure 1.

Biodegradable μtanks were fabricated from PVA and PLGA

Polymers have intrinsic permeabilities to O_2 and other gases. In order to determine ideal candidates for μtanks, a thorough review of the literature was conducted to compare the diffusion coefficients of biodegradable polymers. It was determined that polyvinyl alcohol (PVA) has one of the lowest permeability values ($2.36*10^{-12}$ $cm^3/cm^2*s*mmHg$[26]) to O_2, an order of magnitude lower than that of polyacrylonitrile used in previous studies[25]. However, PVA is sensitive to hydrolysis. To prevent rapid resorption of the PVA layer, we used water/oil/water double emulsion solvent evaporation to create a solid poly(lactic-co-glycolic acid) (PLGA) layer around the outer surface of the hollow PVA layer (Supplemental Fig. 2, Fig. 1A). Several μtank formulations were tested via a one-factor-at-a-time experimental design to obtain spherical, hollow, intact particles that could withstand subsequent hyperbaric loading and 3D-printing (Supplemental table 2, Fig. 1B–D). There were multiple procedures that produced intact μtanks, however the formulation used for further studies was chosen because the size was slightly larger (average diameter of 8.7±4.5 μm) than the others. This is important because μtank size is a critical determining factor in how much O_2 can be dissolved into scaffolds[25,27].

PCL-μtank scaffolds were successfully 3D-printed with up to 20% μtanks (by weight)

Next, we established the effects of μtank incorporation into 3D-printed scaffold surface morphology and print quality (Fig. 1E). Lyophilized μtanks were mixed at varying concentrations (0–20% μtank wt/wt) with PCL powder and extruded through a custom pneumatic printer. We observed minimal changes in surface architecture by SEM (Fig. 1F–H). The overall structure of scaffold sheets were rectilinear patterns with an infill density of 40% (Fig. 1I–J). All three concentrations could be printed using our setup, and printing at higher concentrations of μtanks was later achieved using a Lulzbot filament extrusion printer (data not shown). 'Print quality' has been assigned as a parameter to compare the ideal design geometry with the print geometry. When compared to the ideal geometry (indicated by the horizontal dotted line showing theoretical pore area and strut thickness based on the CAD design) and quantified from a top-down view, we determined that 20% μtanks had significantly higher deposition error or lower print quality than 0% or 10% μtank scaffolds, which was largely due to over-extrusion of materials resulting in smaller pore area (Fig. 1K–L). Improved optimization of extrusion rate and linear print speed to account for possible changes in thermal properties due to increased μtank concentration might alleviate the reduction in print quality.

Increases in μtank concentration and hyperbaric loading pressure increase cumulative O_2 loading and period of O_2 release

Temporal O_2 release kinetics were measured using a Seahorse XF Flux Analyzer and O_2 release period and cumulative O_2 loading were calculated from the O_2 delivery rate traces (Fig. 2A). The cumulative releases (Fig. 2B) and release periods (Fig. 2C) for scaffolds containing 20% μtank were higher than those of any other μtank concentration at every loading pressure. There appeared to be a mild positive relationship between μtank concentration and cumulative loading. Oxygen release kinetics can be tuned by altering μtank concentration and hyperbaric loading pressure. Both μtank concentrations and loading pressures significantly affect the cumulative oxygen loading of the scaffolds (via two-way ANOVA, $p < 0.0001$ and $p = 0.0067$ respectively). For release periods, the microtank concentrations did not induce statistically significant differences ($p = 0.052$), though the increase in loading pressure had a significant impact ($p = 0.0072$) There was a slight trend of increased cumulative O_2 loading and release period with increasing loading pressures. This was more evident at higher μtank concentrations, possibly due to the increased amounts of void volumes within the scaffold struts.

Adipose derived stem cells demonstrated increased HIF-1α expression and decreased osteogenic differentiation in hypoxia

To validate the O_2-dependent effects on osteogenesis, passage 2 (P2) hASCs were cultured in osteogenic media for 1 week in 0.2%, 1%, or 20% O_2. Gene expression levels for HIF-1α and Runx2 and alkaline phosphatase activity were measured at the end of the culture period. Hypoxia upregulated HIF-1α (Fig. 3A) expression in a dose-dependent manner while both moderate and severe hypoxia downregulated Runx2 expression (to similar levels) (Fig. 3B) and alkaline phosphatase activity (Fig. 3C). These data suggest that hypoxia and HIF-1α expression negatively impacted osteogenic differentiation of hASCs *in vitro*.

Adipose derived stem cells did not exhibit long term damage due to short-term hyperoxia

The hASCs were seeded in fibrin hydrogels within the pore spaces of 4 mm Ø x 0.5 mm thickness cylindrical 3D-printed 10% μtank scaffolds that were either not loaded (i.e. Unloaded) or hyperbarically loaded for 1 week with O_2 (i.e. O_2-loaded) at 500 psi. DNA content was measured at 1, 3, and 7 days and normalized to the initial amount of DNA in each scaffold. A slight increase in DNA content between Unloaded and O_2-Loaded μtank scaffolds was observed after 24 hours, suggesting that O_2 loading may help initial proliferation or cell viability, but after several days this effect was abated (Fig. 4A).

Intracellular hydrogen peroxide concentration can be used by cells as a signaling molecule or an indicator of cellular stress depending upon the local concentration[28]. To measure intracellular hydrogen peroxide, hASCs were transfected with a HyPer-3 genetic sensor that changed fluorescence lifetime in the presence of hydrogen peroxide: shorter fluorescence lifetimes indicated higher intracellular hydrogen peroxide concentrations[29]. There were no significant differences in fluorescent lifetime between Unloaded and O_2-Loaded μtank scaffolds, suggesting that the initial burst of O_2 from the scaffolds does not result in persistent intracellular stress (Fig. 4B).

The unloaded and O_2-loaded 3D-printed μtank scaffolds loaded were further employed to evaluate the effect of O_2 release on early-stage osteogenic differentiation markers (Fig. 4C–D). hASC-seeded scaffolds were cultured in osteogenic medium for 2 and 7 days, and PCR was carried out to measure relative mRNA expression of *Runx2* and *ALPL* (alkaline phosphatase) genes normalized to unloaded 3D-printed μtank scaffold control. O_2-loaded 3D-printed μtank scaffolds showed statistically significant increase ($p<0.001$) in *Runx2* expression at as early as 2 days. The *Runx2* expression at day 7 was lower in the O_2-loaded group suggesting peak *Runx2* expression might have already occurred. The day 2 *ALPL* data was inconclusive, but we found that at day 7 ALPL mRNA expression was significantly elevated in the O_2-loaded group further suggesting that O_2 release might be accelerating osteogenic differentiation.

In order to discern how hASCs might be responding to short term supraphysiological O_2 tensions, we cultured P2 hASCs in ambient (20%) and 100% O_2 for 2 and 24 hours and analyzed the expression of common genes associated with the antioxidant response[30]. Increases in ROS expression stimulate NRF-2α and SIRT3, which can upregulate the transcription factor FOXO3, and subsequently upregulate the enzymes involved in removal reactive O_2 species such as superoxide dismutase-2 (SOD2)[30], as represented in Fig. 5A. We observed slight (though not statistically significant) upregulation of the genes NRF-2α (Fig. 5B) and SIRT3 (Fig. 5C) at 2 hours and upregulation of (SOD2) at 24 hours (Fig. 5D). There was no observed change in SOD1 or Catalase at the time points measured (Fig. 5E–F)

O_2 delivery improved deposition of osteogenic proteins and extracellular matrix in murine calvarial defects

To determine the effects of O_2 delivery on regeneration in orthotopic bone defects, the murine calvarial defect model was used (Supplementary Fig. 3). We fabricated PCL-μtank scaffolds and included decellularized bone (DCB) in the struts. The scaffolds were

either not loaded (i.e. Unloaded) or loaded hyperbarically with O_2 (i.e. O_2-Loaded) for 1 week at 500 psi. These scaffolds were combined with hASCs *in situ* in a 4 mm diameter defect through the entire thickness of the mouse calvaria. Following 8 weeks of implantation, microcomputed tomography (μCT) was used to measure differences in mineral deposition between Unloaded and O_2-Loaded groups (Fig. 6A–B, Supplementary Fig. 4). No significant differences in bone volume increase or bone surface area were observed, though we did observe increased mineralization in the O_2-Loaded group (Fig. 6C–D). Further, we sectioned through the calvaria and performed H&E and Masson's trichrome staining of the extracellular matrix (ECM). We observed qualitatively in both the H&E and Masson's trichrome that the ECM appeared to be denser in the O_2-Loaded samples compared to the unloaded samples (Fig. 6E–H). Samples were stained for osteopontin, a mature marker for osteogenesis (Fig. 6I–J). It was found that both the osteopontin area coverage (Fig. 6K) and the signal intensity (Fig. 6L) was greater in O_2-loaded groups than unloaded groups, using the same imaging parameters for both groups. Finally, sections were stained for human Lamin A+C to determine hASC cell survival and CD31 to characterize the presence of endothelial cells in the defects. No significant differences in either hASCs (Supplementary Fig. 5) or CD31 area coverage (Supplementary Fig. 6) were observed in this study.

For this study, we not only examined total mineral deposited, but also spatial distribution of mineralized tissue through the calvarial defects. By segmenting out the native host bone and scaffold, we were able to extract bony nodules that grew inside the defect region. In the calvarial defect, we found that bone primarily formed along scaffold struts, but in O_2-Loaded scaffolds more bone nodules could be found at increasing average distance from the struts (Figure 7). This difference is modest, approximately the size of a few cell layers, but it is possible that an increase in oxygen release could further improve this metric. In this figure, distances >400 μm were primarily located on the periphery outside of the scaffold area.

O_2 delivery improved mineralization and osteogenic protein deposition in murine subcutaneous defects

As there were no statistically significant differences in the amount of mineral deposited in the calvarial defects, but striking differences between the amount of extracellular matrix and osteopontin were observed, we hypothesized that the mouse calvarium may be too thin to observe O_2 gradients, though other groups have found mouse calvaria are hypoxic (1–4% O_2) overall[31,32]. Thus, we investigated the effect of O_2 delivery on mineralization in larger volume defects in mouse dorsal subcutaneous pouches (Supplementary Fig. 7). In this study, 4 × 4 × 8 mm PCL-μtank Unloaded or O_2-Loaded scaffolds were seeded with osteogenically pre-differentiated hASCs and decellularized bone (to promote osteogenesis) in the pore spaces and implanted subcutaneously into mice (n = 8 scaffolds/group, each mouse with 4 defects). We took μCT measurements of initial samples to measure the amount of mineral in the grafts for comparison to endpoint samples. After 8 weeks, implants were excised and imaged (Fig. 8A) and a significant increase in bone volume (Fig. 8B) and osteopontin coverage (Fig. 8C–D) were observed in the O_2-Loaded groups. Scaffolds from both groups had vascular structures with red blood cells (Supplementary Fig. 8), but no quantitative

difference in hASC presence (Supplementary Fig. 9) or CD31 staining (Supplementary Fig. 10) was observed in this study.

Further, we segmented analyzed bone particular distribution within our subcutaneous defects and found similar trends as in the calvarial defects: bone nodules tended to be slightly farther from scaffold struts in the O_2-Loaded scaffolds than unloaded (Figure 9A–E), encompassing the pore spaces. Some nodules form on the periphery at distances greater than half the average pore space. There were slight but significant differences in the average bone nodule volume and surface area, with those from the unloaded group being slightly larger (Figure 9B–C), but a non-significant trend of a greater number of particles per scaffold in the O_2-loaded group (**9D**).

Discussion

Previous studies examining the effects of O_2 delivery on bone regeneration have either focused on systemic delivery using hyperbaric O_2 therapy or delivery of perfluorocarbons within hydrogels, with reports of increased O_2 tension resulting in improvements in bone regeneration[13–16,33–35]. The findings from our study using local O_2 delivery from the thermoplastic scaffold struts were consistent with these other studies, while providing a more facile approach than repeated O_2 administrations required by hyperbaric oxygen therapy and a more mechanically robust scaffold than previous efforts using perfluorocarbons in hydrogels. Craniofacial bone defects are particularly difficult to treat as the regenerated bones should be capable of withstanding the significant forces needed for mastication while successfully recapitulating the native aesthetics and bone contours that impact facial appearance[23]. Extrusion-based 3D-printing allows for the precise control of scaffold deposition, allowing for design of macro-geometry, micro-architecture, bioactivity, and mechanical properties[36–39]. Here, we assessed a novel modification that incorporates O_2-releasing μtank particles into 3D-printed scaffolds and demonstrate a modest, yet positive effect of short-term O_2 delivery on bone regeneration.

Porous μtank scaffolds provided a modest period of O_2 release (~ 8 hours) compared to other methods such as perfluorocarbons, peroxides, and other microparticle-based strategies. Perfluorocarbons such as perfluorotributylamine were shown to have release periods of 96–144 hours when encapsulated in alginate beads or PCL fibers[34,40]. Calcium and manganese peroxide incorporated into microparticles were shown to have release periods of approximately 96 hours[41]. Thus, more direct comparisons between the pro-osteogenic effects of μtank-mediated release and these other methods may rely on longer O_2 release profiles which would require us to fabricate larger μtanks with thicker shells[27]. The bulk emulsion process for fabrication of PVA-PLGA μtanks did not allow for tight control of diameter or shell thickness of the particles and resulted in relatively polydisperse particles. The maximum average diameter we achieved was 8.7±4.5 μm and is similar to what other groups have reported for PLGA particles[42]. However, this was significantly smaller than the commercially available polyacrylonitrile particles used in our previous study (50–100 μm diameter)[25]. In spite of this, the release kinetics of the 3D-printed porous scaffolds was similar to what we observed from commercially available polyacrylonitrile μtanks incorporated into 1 mm height x 3 mm diameter solid polycaprolactone discs[25], even

though the porous scaffolds had significantly increased surface area available for O_2 escape. It is unclear whether this is due to the order of magnitude lower permeability of PVA to O_2 (~2.36×10^{-12} $cm^3/cm^2\cdot s\cdot mmHg$) compared to polyacrylonitrile (~2.36×10^{-11} $cm^3/cm^2\cdot s\cdot mmHg$ for PAN[26,43]) or to the more sensitive methods used to assess O_2 release in this study. Future studies will investigate microfluidics approaches and optimization via multi-target experimental design to control both μtank diameter and shell thickness. We have successfully 3D-printed larger, commercially available polyacrylonitrile μtanks in PCL scaffolds at similar concentrations to demonstrate the feasibility of this process.

Interestingly, the positive effects on bone regeneration with these scaffolds and co-delivered hASCs in both calvarial and subcutaneous defect models were observed 8 weeks after implantation, despite only 8 hours of outgassing. This suggests that even a short period of initial O_2 release could be beneficial for osteogenic outcomes, while potentially avoiding some of the negative systemic side-effects observed from other strategies and maintaining structural integrity. We had initially theorized either enhanced survival of implanted cells (due to a more hospitable microenvironment) or improved vascularization (due to improved vasculogenesis[44,45]) would mediate differences we saw in mineralization after 8 weeks. Additionally, several studies have suggested the tight coupling of angiogenesis and osteogenesis and the importance of O_2 in those processes[44,46,47]; however it appeared that the number of cells and vessel areas in the defects were consistent between groups. In other studies investigating the effect of O_2 delivery on mineralization, no differences in vasculature were observed at day 14 and significant differences in cell survival were only observed at day 3, though osteocalcin expression was elevated throughout from days 5–14[35]. It is quite possible that by 8 weeks, initial differences between the groups in cell survival and vascular density have normalized, through implanted cell proliferation and vascular pruning. In future studies, we will investigate the mechanisms underlying this observed benefit to osteogenesis in our models.

One of the drawbacks of many O_2 delivery strategies, including μtanks, is the bulk release of O_2 and exposing cells to O_2 concentrations much higher than they typically experience *in vivo* or *in vitro*. Thus, we were interested in studying manners in which cells might respond to hyperoxia, primarily through the antioxidant pathway. One of the most prominent antioxidant pathways involves the nuclear factor erythroid-2 (Nrf-2) transcription factors. Nrf-2 is constitutively expressed in the cytosol and translocates to the nucleus during periods of oxidative stress, where it binds to antioxidant response elements and actives gene expression of genes involved in alleviating oxidative stress, including superoxide dismutase and catalase[48] as well as the deacetylase SIRT3[49]. SIRT3 functions in the mitochondria to alter the enzymatic activity of glycolytic enzymes and by activating the transcription factor forkhead box O3a, which in turn activates superoxide dismutase-2 and catalase[50]. There is evidence to suggest that SIRT-3 dependent deacetylation of enzymes such as SOD2 is evident within 24 hours of nutrient starvation, while there is minimal upregulation of SIRT-3 genes until after 24 hours[51]. This could explain why only slight upregulation (not statistically significant) of Nrf-2α and SIRT-3 were observed in response to hyperoxia at 24 hours, as their primary mechanism is through altering the expression of other genes, while SOD2 upregulation was observed within that time frame as it directly acts to convert reactive O_2 species into less damaging states. In this study, it appeared that hASCs were able to

upregulate antioxidant response mechanisms to largely avoid cellular damage caused by an initial, brief period of hyperoxia.

The results of this study open many new avenues for future exploration. Particularly, that the short period of O_2 release could cause observable changes even at 8 weeks post implantation was intriguing and suggests that an understanding of the microenvironment immediately following implantation should be investigated in future studies. To elucidate the mechanisms behind this action, shorter term experiments to interrogate precisely what changes in gene expression or secreted proteins induced by O_2 delivery might lead to differences in end-point mineralization will be useful. Additionally, the development of tighter control of O_2 release kinetics could be achieved using microfluidics in combination with a Design of Experiments approach with multi-target optimization for large diameter and small polydispersity index. The addition of perfluorocarbons or peroxides in the inner layer to extend release could also be investigated to determine appropriate dose of O_2 to achieve maximal bone regeneration. Finally, larger animal models would be necessary to demonstrate scalability of the 3D-printed O_2-releasing scaffolds.

Conclusions

In conclusion, 3D-printed μtank scaffolds were developed and shown to provide modest, but discernable, improvements in osteogenic outcomes in both murine calvarial and subcutaneous defects. There was a trend of increased mineralization and a statistically significant increase in matrix osteogenic protein deposition which suggested that O_2 delivery had an effect on the regenerating bone tissue. In subcutaneous defects where the volume of scaffolds was larger, O_2 delivery promoted both mineralization and osteogenic protein deposition. Future studies will investigate the changes elicited in hASCs by O_2 delivery that could result in these positive outcomes, improve upon the μtank polydispersity to understand dose-dependency of O_2 delivery, and scale up to larger animal models.

Materials and Methods:

μtank Fabrication

μtanks were formulated using a water-oil-water double emulsion, with a primary emulsion of 15 mL of 10% polyvinyl alcohol (30–70kDa and 87–90% hydrolyzed, Sigma Aldrich) in deionized water and 30 mL 7% 50:50 25–35kDa poly(lactic-co-glycolic acid) (PLGA) (Polyscitech, West Lafayette, IN) in dichloromethane (Sigma Aldrich) stirred, covered, at 500 rpm for 1 hour. The primary emulsion solution was added slowly to a 100 mL 1% gelatin (Sigma Aldrich) solution in water to form a secondary emulsion. This solution was stirred, uncovered, overnight to allow for evaporation of the dichloromethane from solution, leaving behind a PLGA layer. μtanks were then filtered through a 100 μm cell strainer and washed in deionized water. Centrifugation at 1000 rpm for 10 minutes allowed for collection of the μtanks from the solution. After three washes in water, the μtanks were frozen at −20°C, lyophilized, and stored at room temperature.

μtanks were imaged using a Zeiss Axio Observer (Oberkochen, Germany) fluorescent wide field microscope platform and average diameters were quantified using a custom MATLAB script.

Scanning electron microscopy

Samples were sputter-coated with Au-Pd at a thickness of 30 nm. Scanning electron microscopy was completed on a LEO 1530 Field Emission SEM (Zeiss, Oberkochen, Germany) at a conductivity of 1 kV.

3D-printing

Scaffolds were 3D printed using a custom pneumatic printer as previously described[39]. μtanks were mixed with PCL powder (Polysciences Inc., Warrington, PA) at percentages of 0%, 10%, and 20% (PVA/PLGA μtanks: PCL mass/mass). Scaffolds had a rectilinear infill pattern with a designed porosity of 60%. The powder mixture was heated to 120°C, at which point the PCL powder melts. The molten scaffold material is forced out of a 0.46 mm nozzle using a custom pneumatic printing system as previously described[39,52]. The print head moves relative to the bed surface, creating a custom 3D pattern. Surface morphology was observed using SEM.

Print quality analysis

Scaffolds were imaged ($n > 6$) on a Zeiss SteREO Discovery stereomicroscope at 1.6x magnification from a top-down view. A custom MATLAB script was written to threshold and analyze print quality. First, images were thresholded using Otsu's Method and then converted to binary. Boundaries and center points of each pore were calculated. To determine strut thickness, for each pore, distances were calculated to all adjacent pores in the horizontal and vertical directions. In addition, each pore was compared against the ideal sized pore (800 μm x 800 μm) drawn automatically by the program from the center point.

Hyperbaric O_2 loading

Scaffolds are hyperbarically loaded in a custom hyperbaric oxygen chamber as previously described[25]. Scaffolds are placed within the chamber and the apparatus is flushed with 100% O_2. After this, the pressure is elevated to 300–500 psi for a period of 1 week. For all experiments, the time between chamber release and scaffold measurements were recorded and incorporated into the release kinetics calculations.

Temporal O_2 release measurements

O_2 release was measured from 0%, 10%, and 20% μtank-PCL scaffolds hyperbarically loaded at 300, 400, and 500 psi for 1 week using a Seahorse XF Flux analyzer (Agilent Technologies, Santa Clara, CA) at 37°C. Scaffolds had a 4 mm diameter, 40% infill, and weighed 6.9 ± 2.4 mg. Cumulative release was determined by integrating the release curve over the time of measurement. The release period is calculated by fitting an exponential curve $\left(y = a * e^{-\lambda t}\right)$ to the release curve, finding the time constant of release (λ), and using

the time constant to calculate the period of time before solution reaches equilibrium (192 μM).

Cell isolation and culture conditions

Human lipoaspirate from subcutaneous adipose tissue was acquired from patients undergoing elective surgery, with written informed consent, and with Institutional Review Board approval (IRB00120495). hASCs were isolated as previously described[53]. Briefly, lipoaspirate was washed with phosphate buffered saline, digested using collagenase type 1 (1mg/mL; Worthington Biochemical Corp., Lakewood, NJ), and centrifuged to collect mesenchymal cells. The cells were plated onto tissue culture plastic and grown to 80–90% confluence before passaging. Growth medium consisted of high glucose DMEM (4.5 mg/mL glucose, Gibco) with 10% fetal bovine serum (Atlanta Biologicals, Flowery Branch, GA), 1% penicillin/streptomycin (Gibco), and 1 ng/mL basic fibroblast growth factor (FGF-2; Peprotech, East Windsor, NJ). Osteogenic media consisted of low glucose DMEM (1 mg/mL glucose, Gibco) with 10% fetal bovine serum, 1% penicillin/streptomycin (Gibco), 10 mM β-glycerophosphate (Sigma Aldrich), and 50 μM ascorbic acid (Sigma Aldrich).

Polymerase Chain Reaction

After the 7-day culture period in varying O_2 tensions using sealed chambers, samples of ASC monolayers (n = 6) have been characterized for PCR. PCR is also carried out for O_2-loaded, hASC-seeded, PCL-μtank scaffolds after 2 and 7 days of culture in hypoxic condition. were digested with TRIzol (Life Technologies, Carlsbad, CA). RNA was extracted from the sample using chloroform and precipitated using isopropanol. Precipitated mRNA was washed in ethanol and dried. After rehydration, the RNA concentration was measured using a NanoDrop 2000 Spectrophotometer (ThermoFisher Scientific, Waltham, MA) and all samples were adjusted to 100 ng/μL. Reverse transcription was performed using the Bio-Rad iScript cDNA synthesis kit (Bio-Rad, Hercules, CA) on a T100 Thermocycler (BioRad, Hercules, CA). cDNA was subject to real-time polymerase chain reaction using the Power SYBR Green Master Mix (ThermoFisher Scientific, Waltham MA) as the fluorescent probe using a StepOnePlus RT-PCR machine (Applied Biosystems, Waltham, MA). The sequences for the forward and reverse primers used are presented in Supplementary Table 1. For analysis, the delta/delta Ct method was used, in which β-actin and GAPDH served as the housekeeping gene, and gene expression was normalized to that of hASCs in normoxic standard culture conditions at day 7. In case of O_2-loaded, hASC-seeded, PCL-μtank scaffolds, gene expression was normalized to unloaded hASC-seeded, PCL-μtank scaffolds. Technical duplicates were averaged before normalization.

Alkaline Phosphatase Activity

Cells in monolayer (n = 6) exposed to different levels of O_2 for 7 days were lysed using a solution 1% Triton-X-100 (Sigma Aldrich, St. Louis, MO), 0.5% sodium deoxycholate (Sigma Aldrich, St. Louis, MO), 0.1% sodium dodecyl sulfate (Sigma Aldrich, St. Louis, MO), 0.1 mg/mL phenylmethanesulfonyl fluoride (Sigma Aldrich, St. Louis, MO), and 0.3% aprotinin from bovine lung (Sigma Aldrich, St. Louis, MO) in deionized water. Cells were snap frozen at −80°C and thawed three times, sonicated, and centrifuged at 13,000g to

obtain both free and membrane-bound alkaline phosphatase. Activity was measured using para-nitrophenyl phosphate color change (Sigma Aldrich, St. Louis, MO), measured using a BioTek Synergy 2 plate reader (BioTek, Winooski, VT) at 405 nm and compared to dephosphorylated para-nitrophenol (Sigma Aldrich, St. Louis, MO) as a standard.

Scaffold seeding

Cells were suspended in fibrinogen (8 mg/mL final; Sigma Aldrich) and then mixed with thrombin (2 U/mL final; Sigma Aldrich) for a final cell concentration in the hydrogel of 10–20,000 cells/μL. Scaffolds were seeded by pipetting 10 μL of gel and cell solution into 4-mm-diameter scaffolds prior to gelation and incubating at 37°C for 10–30 minutes to allow complete gelation before the addition of medium or implantation into animals.

DNA content

To determine the effect of O_2 delivery on ASC proliferation, cellular DNA content was assessed using the Quant-It PicoGreen dsDNA assay (Invitrogen, Carlsbad, CA) following the manufacturer's instructions.

HyPer-3 sensor and confocal fluorescence lifetime imaging microscopy

The genetically encoded fluorescent biosensor HyPer-3 (Addgene plasmid #42131, Addgene, Watertown, MA) under control of a constitutive CMV promotor was used for measuring hydrogen peroxide concentrations inside living hASCs[29,54]. hASCs were transfected with HyPer-3 sensor using a poly(β-amino ester): N'-(2-((3-animopropyl)animo)ethan-1-ol) end-modified poly(1,4-butanediol diacrylate-co-animo-1-butanol) (referred to as PBAE 44E6) as previously described[55,56]. Briefly, hASCs were cultured in monolayer. Immediately before transfection, media was changed to 2 ml/well of serum-free high-glucose DMEM with pyruvate (Gibco). PBAE 44E6 and HyPer-3 DNA (pC1-HyPer-3) were both diluted in 25 mM sodium acetate buffer (pH 5; NaAc, Sigma Aldrich) and mixed at polymer-DNA ratios of 60 w/w. The Polymer-DNA nanocomplexes were allowed to form for 10 min. Cells were then transfected by adding 200 μL nanocomplexes to each well at a final dose of 7 μg DNA/well and incubated for 2 h at 37°C and 5% CO2. After 2 h, the media was changed to original serum-containing growth media.

Two days following transfection and upregulation of HyPer-3, cells were harvested and pooled with non-transfected hASCs at a ratio of 1:10. Pooled cells were encapsulated in fibrin hydrogels within the pore spaces of unloaded or hyperbarically-loaded 10% μtank scaffolds. Confocal fluorescence lifetime imaging microscopy (FLIM) of hASCs containing the HyPer-3 biosensor was performed utilizing a Zeiss LSM 780 microscope (Zeiss, Oberkochen, Germany) and PicoQuant (PicoQuant, Berlin, Germany) system equipped with the PicoHarp 300 time-correlated single photon counting (TSPC) module, hybrid PMA-04 detector, and Sepia II laser control module. Cell seeded scaffolds were maintained in a Pecon environmental chamber at 37°C and 5% CO_2. Before FLIM acquisition, a single confocal image at 1024 × 1024 pixel size was obtained of the transfected HyPer3 hASCs within the scaffold using an Apochromat x40/1.1W Corr 27 lens (Zeiss, Oberkochen, Germany), excitation with PicoQuant 485 nm pulsed diode laser (32.5 MHz) and the

Zeiss780 GaAsP detector to capture circularly permuted yellow fluorescent protein (cpYFP, built into HyPer3) emission and the transmitted light detector to acquire differential interference contrast (DIC) images. FLIM data was collected from the same location utilizing the same objective, frame size, and laser. The pinhole size was adjusted for each image to acquire data from 2 to 4 μm z-sections to limit the emission photon rate below 10% of the laser excitation rate. FLIM images were acquired with a 58.2 μs pixel dwell time.

FLIM data were processed with SymPhoTime (PicoQuant, Berlin, Germany) software, using a customized script for the calculation of the internal response function from 1000 data points with no smoothing. The acquired data were binned to obtain at least 600 photons per binned pixel and the out-of-cell fluorescence was removed by applying a cell-specific threshold. A three-exponential reconvolution was used to fit the fluorescence decays into every binned pixel. Subsequently, the amplitude-weighted fluorescence lifetime averages in different scaffold areas were calculated with SymPhoTime.

Subcutaneous murine defect

For the subcutaneous mouse study, 8 mm x 4 mm x 4 mm scaffolds with 60% void volume were printed with 10% μtanks and hyperbarically loaded at 500 psi for 7 days. Passage 2 human hASCs were pre-differentiated in osteogenic media containing 20 ng/mL of platelet-derived growth factor for 5 days. hASCs were seeded in the scaffold pore spaces along with decellularized bone particles (40 mg/mL) within a fibrin gel carrier at a concentration of 20,000 cells/μL, as previously described[39,52,53]. Pre-differentiation and decellularized bone particles were utilized because the subcutaneous defect is not naturally osteogenic and we wanted to determine the effect of O_2 release in large scaffolds *in vivo*.

In conducting research using animals, the investigators adhered to the laws of the United States and regulations of the Department of Agriculture. All studies were approved by the Johns Hopkins University Institutional Animal Care and Use Committee (MO19M150). Male nude homozygous Nu/J mice (The Jackson Laboratory, Bar Harbor, ME) were used at 8 weeks of age. Scaffolds were implanted in four positions in dorsal subcutaneous defects for a total of 8 weeks before sacrifice. Animals were then euthanized using CO_2 inhalation. Samples were excised and fixed in 4% paraformaldehyde overnight for further analysis. Post-mortem imaging of defects with computed tomography (CT) used a nanoScan PET/CT (Mediso, Budapest). Imaging was performed at 35 kV peak voltage and 800 μA current (0.48mAs). Reconstruction was done with a voxel size of 40 μm.

Calvarial defect

A bilateral 4-mm critically-sized murine calvarial defect model was utilized to assess bone regeneration following a protocol approved by the Johns Hopkins University Institutional Animal Care and Use Committee (MO18M188). To determine the effect of O_2 delivery on bone regeneration *in vivo*, 20% μtank-30% DCB-PCL scaffolds were implanted either with or without hyperbaric O_2 loading for 1 week at 500 psi. Eight week-old, male, homozygous Nu/J mice (The Jackson Laboratory, Bar Harbor, ME) were initially weighed and anesthetized via a single intraperitoneal injection with ketamine and xylazine. The paw-pinch test was performed to determine the level of sedation. For sustained analgesia

during the procedure, 0.2 mg kg^{-1} of buprenorphine was subcutaneously injected. Then, the mice's heads were placed on a stereotactic frame (900LS, David Kopf Instruments, Tujunga, CA) to stabilize the skull. The skin was treated with alcohol and betadine. Sterile gloves were used by all surgical personnel, while all the surgical procedures were performed under an operating microscope (NC-4 Carl Zeiss, Oberkochen Germany) by a single surgeon. A mid-sagittal incision was made over the calvarium and sterile cotton swabs were used to gently remove the pericranium at the defect site. Following identification of anatomical landmarks, two 4-mm defects were made in the parietal bone of the calvarium using an Ideal Microdrill (Harvard Apparatus, Holliston, MA). Each defect was created 1 mm away from the sagittal suture and equidistant from the coronal and lambdoid sutures. Care was taken to preserve the underlying dura mater. Scaffolds were placed in one of the defects, leaving the contralateral side empty as a control. Scaffolds were seeded with cells suspended in fibrin hydrogels (fibrinogen, Sigma Aldrich, 10 mg/mL, 10 μL total volume, 10,000 cells/μL) and allowed to polymerize for at least 2 minutes before incisions were closed with 6–0 nylon sutures. Mice were treated with subcutaneous injections of 0.2 mg kg^{-1} buprenorphine on each of the two days following surgery for pain management. Mice were monitored daily up to one week following procedure for any neurological deficits, infection, or distress.

At 8 weeks post-implantation, mice were euthanized using CO_2 inhalation and calvaria were harvested and fixed in 4% paraformaldehyde. Calvaria were scanned using a Bruker Skyscan 1275 μCT (Billerica, MA) to assess bone mineral deposition. Scans were performed with a 1 mm aluminum filter at 65 keV and with 0.3° rotation between images. The resulting image resolution was 10 μm. 3D rendering and bone volume quantification in the defects was performed using Mimics 14 Software (Materialise, Leuven, Belgium). Grafts that displaced from the defect removed from subsequent analysis.

Analysis of bone distribution:

CT data analysis was performed using Avizo (FEI Visualization Sciences Group, Burlington, MA). Labels for native tissue, scaffold, and new bone formation in the defect region were created using the threshold and watershed tools. Spatial distribution of bone formation inside scaffold was extracted using the label analysis function. Distance maps were generated for all voxels within each bone nodule to find the average distance from each bone nodule to the closest scaffold strut.

Histology:

Samples from subcutaneous and calvarial defects were embedded in paraffin and sectioned at a 4 μm thickness for subsequent histological analysis. Slides were hydrated using an ethanol gradient and stained with H&E and Masson's trichrome (Mastertech Stains, StatLab, McKinney, TX) or processed further for immunofluorescent staining.

Fluorescent Immunostaining:

Slides were re-hydrated using a graded ethanol ladder. To improve signal-to-noise ratio, slides were incubated in Antigen Retrieval Buffer (100X Tris-EDTA, Abcam, Cambridge, UK) at 212°C in a water bath for 20 minutes. After cooling, slides were blocked and permeabilized for 30 minutes with 0.2% Triton X-100, 10% normal goat serum (Sigma

Aldrich). Scaffolds were then incubated with primary antibodies for CD31 (R&D Systems, Minneapolis, MN, goat α mouse, AF3628), lamin A-C (Abcam, Cambridge, UK, rabbit α human, ab108595), osteopontin (R&D Systems, Minneapolis, MN, rat α human, MAB808–100), rabbit anti-CD86 (1:50; Thermo Fisher), goat anti-CD206 (1:50, Santa Cruz) in 10% normal goat serum in 0.2% Tween in PBS overnight, followed by three 5 minute washes in PBS. Secondary antibodies (donkey α goat 488+, ThermoFisher; donkey α rabbit AF647+ for lamin A-C and ThermoFisher; donkey α rabbit AF555, ThermoFisher) were then diluted 1:100 in 10% normal donkey serum along with DAPI (1:2000) for 1 hour at room temperature. Samples were washed three times in PBS before mounting with 50% glycerol and sealed.

Slides were imaged on a Zeiss Z2 Axio Observer with Apotome (Zeiss, Oberkochen, Germany). All staining on *in vivo* samples was performed with n = 3–4 samples per group and each sample had 5–6 slides imaged. To quantify human cells, the lamin A-C stain was quantified and overlaid with DAPI in the defect area using a custom MATLAB script. Areas of CD31 and OPN staining in the defect regions were quantified using custom MATLAB script.

Statistical Methods

Quantitative data are expressed as the mean ± standard deviation. Statistical analyses were performed using GraphPad Prism 5 software. Statistical analysis for print quality, ASC gene expression was carried out by one-way ANOVA with Bon-Ferroni post-test. DNA content, intracellular hydrogen peroxide, antioxidant gene expression was conducted using a two-way ANOVA with Bon Ferroni post-test. Bone volume, protein deposition, bone nodule quantification, vessel quantification, and human cell retention were analyzed using an unpaired two-tailed t-test. Throughout the study, statistical significance has been denoted as *($p < 0.05$), **($p < 0.01$) and ***($p < 0.001$).

Supplementary Material

Refer to Web version on PubMed Central for supplementary material.

Acknowledgements

We would like to thank David Wilson from Dr. Jordan Green's lab for generously providing PBAE nanoparticles and conducting training for transfection. Funding for this project was provided by the National Science Foundation Graduate Research Fellowship (ALF), NIH National Institute for Arthritis and Musculoskeletal and Skin Diseases Grant No. 1 F31 AR075368 (ALF), NIH National Institute for Dental and Craniofacial Research Grant No. 5 R01 DE027957-02 (WLG), and the Research Foundation - Flanders for the post-doctoral fellowship 12I6216N (D.L.), grant no. 1516517N (D.L.) and travel grant no. V437017N (D.L.).

References:

1. Chen D. et al. Tissue engineered autologous cartilage-bone grafts for temporomandibular joint regeneration. Sci. Transl. Med 12, (2020).
2. Bhumiratana S. et al. Tissue-engineered autologous grafts for facial bone reconstruction. Sci. Transl. Med 8, 343–83 (2016).

3. Mulloy C. et al. Experimental Model of Zygomatic and Mandibular Defects to Support the Development of Custom Three-Dimensional--Printed Bone Scaffolds. J. Craniofac. Surg 31, 1488–1491 (2020). [PubMed: 32541268]
4. Tatara AM et al. Reconstruction of large mandibular defects using autologous tissues generated from in vivo bioreactors. Acta Biomater. 45, 72–84 (2016). [PubMed: 27633319]
5. Vidal L. et al. In situ production of pre-vascularized synthetic bone grafts for regenerating critical-sized defects in rabbits. Acta Biomater. 114, 384–394 (2020). [PubMed: 32688088]
6. Stegen S. et al. HIF-1α promotes glutamine-mediated redox homeostasis and glycogen-dependent bioenergetics to support postimplantation bone cell survival. Cell Metab. 23, 265–279 (2016). [PubMed: 26863487]
7. Hutton DL, Moore EM, Gimble JM & Grayson WL Platelet-Derived Growth Factor and Spatiotemporal Cues Induce Development of Vascularized Bone Tissue by Adipose-Derived Stem Cells. Tissue Eng. Part A 19, 2076–2086 (2013). [PubMed: 23582144]
8. Li J, Jahr H, Zheng W. & Ren PG Visualizing angiogenesis by multiphoton microscopy In Vivo in genetically modified 3D-PLGA/nHAp scaffold for calvarial critical bone defect repair. J. Vis. Exp 2017, (2017).
9. Boutilier RG & St-Pierre J. Surviving hypoxia without really dying. Comp. Biochem. Physiol. Part A 126, 481–490 (2000).
10. Lee P, Chandel NS & Simon MC Cellular adaptation to hypoxia through hypoxia inducible factors and beyond. Nature Reviews Molecular Cell Biology vol. 21 268–283 (2020). [PubMed: 32144406]
11. Ishaug SL et al. Bone formation by three-dimensional stromal osteoblast culture in biodegradable polymer scaffolds. J. Biomed. Mater. Res 36, 17–28 (1997). [PubMed: 9212385]
12. Ishaug-Riley SL, Crane-Kruger GM, Yaszemski MJ & Mikos AG Three-dimensional culture of rat calvarial osteoblasts in porous biodegradable polymers. Biomaterials 19, 1405–1412 (1998). [PubMed: 9758040]
13. Pedersen TO, Xing Z, Finne-Wistrand a., Hellem S. & Mustafa K. Hyperbaric oxygen stimulates vascularization and bone formation in rat calvarial defects. Int. J. Oral Maxillofac. Surg 42, 907–914 (2013). [PubMed: 23403337]
14. Kawada S, Wada E, Matsuda R. & Ishii N. Hyperbaric Hyperoxia Accelerates Fracture Healing in Mice. PLoS One 8, e72603 (2013).
15. Grassmann J. et al. Hyperbaric oxygen therapy improves angiogenesis and bone formation in critical sized diaphyseal defects. J. Orthop. Res 33, 513–520 (2015). [PubMed: 25640997]
16. Rocha FS et al. Influence of hyperbaric oxygen on the initial stages of bone healing. Oral Surg. Oral Med. Oral Pathol. Oral Radiol 120, 581–587 (2015). [PubMed: 26324750]
17. Farris AL, Rindone AN & Grayson WL Oxygen delivering biomaterials for tissue engineering. J. Mater. Chem. B 4, 3422–3432 (2016). [PubMed: 27453782]
18. Khattak SF, Chin K, Bhatia SR & Roberts SC Enhancing oxygen tension and cellular function in alginate cell encapsulation devices through the use of perfluorocarbons. Biotechnol. Bioeng 96, 156–66 (2007). [PubMed: 16917927]
19. Palumbo FS et al. Perfluorocarbon functionalized hyaluronic acid derivatives as oxygenating systems for cell culture. RSC Adv. 4, 22894 (2014).
20. Centis V, Proulx P. & Vermette P. PEGylated liposomes encapsulating human hemoglobin enhance oxygen transfer and cell proliferation while decreasing cell hypoxia in fibrin. Biochem. Eng. J 55, 162–168 (2011).
21. Castro CI & Briceno JC Perfluorocarbon-Based Oxygen Carriers: Review of Products and Trials. Artif. Organs 34, no-no (2010).
22. Riess JG Perfluorocarbon-based Oxygen Delivery. Artif. Cells, Blood Substitutes Biotechnol. 34, 567–580 (2006).
23. Nyberg EL et al. 3D-Printing Technologies for Craniofacial Rehabilitation, Reconstruction, and Regeneration. Ann. Biomed. Eng 45, 45–57 (2017). [PubMed: 27295184]
24. Nyberg E, Rindone A, Dorafshar A. & Grayson WL Comparison of 3D-Printed Poly-ε-caprolactone Scaffolds Functionalized with Tricalcium Phosphate, Hydroxyapatite, Bio-Oss, or Decellularized Bone Matrix. Tissue Eng. Part A 23, 503–514 (2016).

25. Cook CA, Hahn KC, Morrissette-McAlmon JBF & Grayson WL Oxygen delivery from hyperbarically loaded microtanks extends cell viability in anoxic environments. Biomaterials 52, 376–384 (2015). [PubMed: 25818444]
26. Mokwena KK & Tang J. Ethylene Vinyl Alcohol: A Review of Barrier Properties for Packaging Shelf Stable Foods. Crit. Rev. Food Sci. Nutr 52, 640–650 (2012). [PubMed: 22530715]
27. Farris AL, Cook CA & Grayson WL Mathematical modeling of oxygen release from hyperbarically loaded polymers. Biotechnol. Prog 35, (2019).
28. Lismont C, Revenco I. & Fransen M. Peroxisomal hydrogen peroxide metabolism and signaling in health and disease. International Journal of Molecular Sciences vol. 20 (2019).
29. Bilan DS et al. HyPer-3: A genetically encoded H2O2 probe with improved performance for ratiometric and fluorescence lifetime imaging. ACS Chem. Biol 8, 535–542 (2013). [PubMed: 23256573]
30. Bause AS & Haigis MC SIRT3 regulation of mitochondrial oxidative stress. Experimental Gerontology vol. 48 634–639 (2013). [PubMed: 22964489]
31. Spencer JA et al. Direct measurement of local oxygen concentration in the bone marrow of live animals. Nature 508, 269–273 (2014). [PubMed: 24590072]
32. Ceradini DJ et al. Progenitor cell trafficking is regulated by hypoxic gradients through HIF-1 induction of SDF-1. Nat. Med 10, 858–864 (2004). [PubMed: 15235597]
33. Sammarco MC et al. Hyperbaric Oxygen Promotes Proximal Bone Regeneration and Organized Collagen Composition during Digit Regeneration. PLoS One 10, e0140156 (2015).
34. Benjamin S. et al. Oxygenated environment enhances both stem cell survival and osteogenic differentiation. Tissue Eng. Part A 19, 748–58 (2013). [PubMed: 23215901]
35. Kimelman-Bleich N. et al. The use of a synthetic oxygen carrier-enriched hydrogel to enhance mesenchymal stem cell-based bone formation in vivo. Biomaterials 30, 4639–4648 (2009). [PubMed: 19540585]
36. Temple JP et al. Engineering anatomically shaped vascularized bone grafts with hASCs and 3D-printed PCL scaffolds. J. Biomed. Mater. Res. Part A 102, 4317–4325 (2014).
37. Hung BP et al. Three-Dimensional Printing of Bone Extracellular Matrix for Craniofacial Regeneration. ACS Biomater. Sci. Eng (2016) doi:10.1021/acsbiomaterials.6b00101.
38. Nyberg E, Rindone A, Dorafshar A. & Grayson WL Comparison of 3D-Printed Poly-ϵ-Caprolactone Scaffolds Functionalized with Tricalcium Phosphate, Hydroxyapatite, Bio-Oss, or Decellularized Bone Matrix. Tissue Eng. - Part A 23, (2017).
39. Rindone AN, Nyberg E. & Grayson WL 3D-printing composite polycaprolactone-decellularized bone matrix scaffolds for bone tissue engineering applications. in Methods in Molecular Biology vol. 1577 (2018).
40. Ma T. et al. Oxygen carrier in core-shell fibers synthesized by coaxial electrospinning enhances Schwann cell survival and nerve regeneration. Theranostics 10, 8957–8973 (2020). [PubMed: 32802174]
41. Hsieh TE et al. Optimizing an Injectable Composite Oxygen-Generating System for Relieving Tissue Hypoxia. Front. Bioeng. Biotechnol 8, (2020).
42. Nguyen T, Peng Y, Seekell RP, Kheir JN & Polizzotti BD Hyperbaric polymer microcapsules for tunable oxygen delivery. J. Control. Release 327, 420–428 (2020). [PubMed: 32798637]
43. Spivack MA & Spivack MA Parylene Thin Films for Radiation Applications. Rev. Sci. Instrum 41, 1614–1616 (1970).
44. Hutton DL & Grayson WL Hypoxia Inhibits De Novo Vascular Assembly of Adipose-derived Stromal/Stem Cell Populations but Promotes Growth Of Pre-Formed Vessels. Tissue Eng. Part A 22, 161–9 (2016). [PubMed: 26481655]
45. Nyberg EL & Grayson WL Assessing the Minimum Time-period of Normoxic Preincubation for Stable Adipose Stromal Cell-derived Vascular Networks. Cell. Mol. Bioeng
46. Nyberg E. & Grayson W. Assessing the Minimum Time-Period of Normoxic Preincubation for Stable Adipose Stromal Cell-Derived Vascular Networks. Cell. Mol. Bioeng 11, 471–481 (2018). [PubMed: 31719894]

47. Merfeld-Clauss S, Gollahalli N, March KL & Traktuev DO Adipose tissue progenitor cells directly interact with endothelial cells to induce vascular network formation. Tissue Eng. - Part A 16, 2953–2966 (2010). [PubMed: 20486792]

48. Ray PD, Huang BW & Tsuji Y. Reactive oxygen species (ROS) homeostasis and redox regulation in cellular signaling. Cellular Signalling vol. 24 981–990 (2012). [PubMed: 22286106]

49. Satterstrom FK et al. Nuclear respiratory factor 2 induces SIRT3 expression. Aging Cell 14, 818–825 (2015). [PubMed: 26109058]

50. Zhang DY et al. Sirtuin3 protects aged human mesenchymal stem cells against oxidative stress and enhances efficacy of cell therapy for ischaemic heart diseases. J. Cell. Mol. Med 22, 5504–5517 (2018). [PubMed: 30091830]

51. Papanicolaou K, O'Rourke B. & Foster DB Metabolism leaves its mark on the powerhouse: Recent progress in post-translational modifications of lysine in mitochondria. Frontiers in Physiology vol. 5 JUL (2014).

52. Hung BP et al. Platelet-Derived Growth Factor BB Enhances Osteogenesis of Adipose-Derived But Not Bone Marrow-Derived Mesenchymal Stromal/Stem Cells. Stem Cells 33, 2773–2784 (2015). [PubMed: 26013357]

53. Nyberg E, Farris A, O'Sullivan A, Rodriguez R. & Grayson WL Comparison of SVF and Passaged ASCs as Point-of-Care Agents for Bone Regeneration. Tissue Eng. Part A ten.TEA.2018.0341 (2019) doi:10.1089/ten.TEA.2018.0341.

54. Belousov VV et al. Genetically encoded fluorescent indicator for intracellular hydrogen peroxide. Nat. Methods 3, 281–286 (2006). [PubMed: 16554833]

55. Sunshine JC, Peng DY & Green JJ Uptake and transfection with polymeric nanoparticles are dependent on polymer end-group structure, but largely independent of nanoparticle physical and chemical properties. Mol. Pharm 9, 3375–3383 (2012). [PubMed: 22970908]

56. Est-Witte SE et al. Non-viral gene delivery of HIF-1α promotes angiogenesis in human adipose-derived stem cells. Acta Biomater. 113, 279–288 (2020). [PubMed: 32623098]

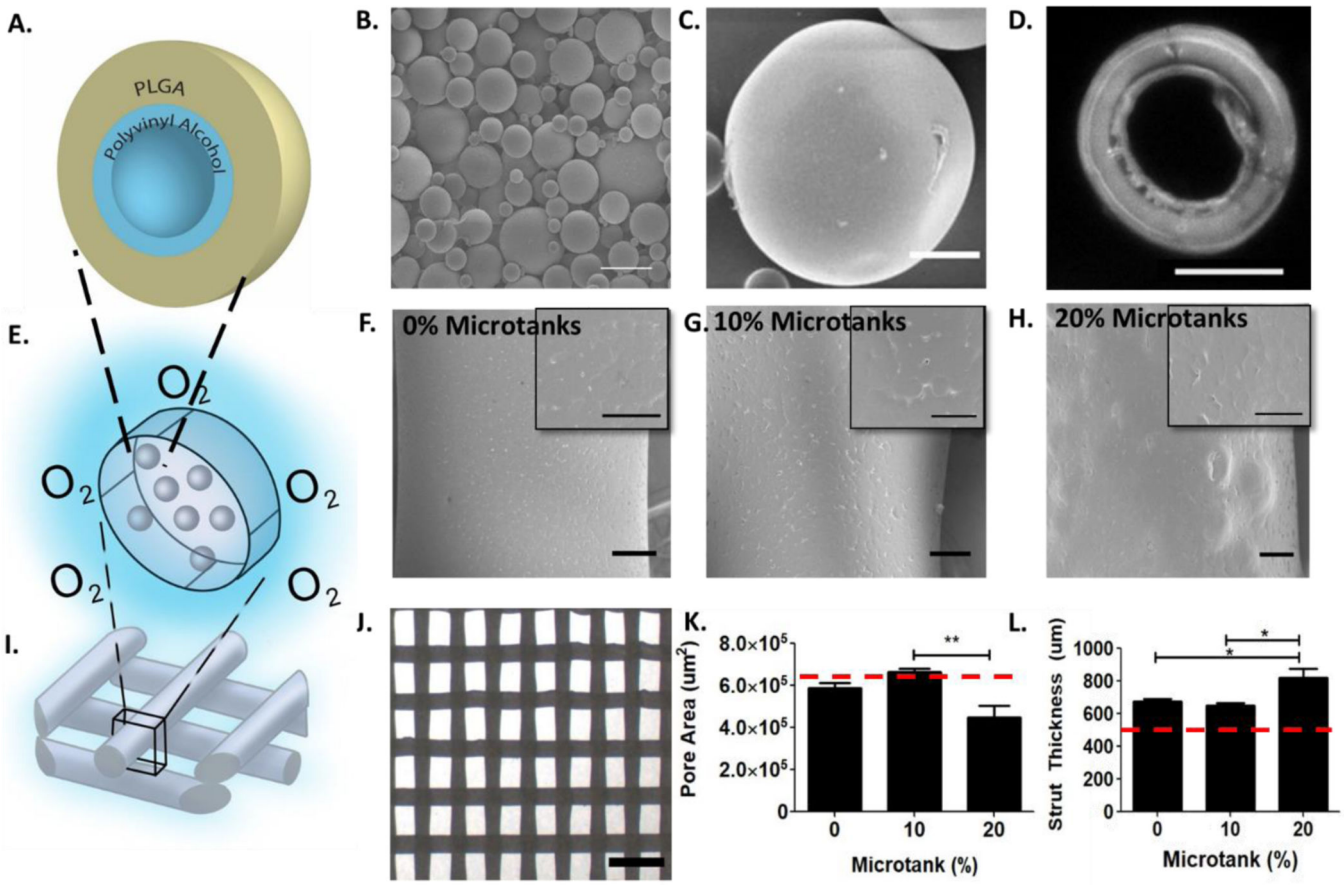

Figure 1: Fabricating and 3D-printing biodegradable PVA/PLGA μtank scaffolds.

(**A**) Schematic depicting theoretical μtank structure. (**B**) Scanning electron micrograph of PVA/PLGA μtanks; Scale bar: 20 μm. (**C**) Scanning electron micrograph of PLGA/PVA μtanks: Scale bar: 10 μm. (**D**) Fluorescence microscope image of a cross-section of a Nile Red fluorescently labeled μtank; Scale bar: 10 μm. (**E**) Schematic of μtanks embedded in PCL scaffold struts. Scanning electron micrographs of PCL scaffold struts containing: (**F**) 0% μtanks, (**G**) 10% μtanks, and (**H**) 20% μtanks. (**F-H**) Scale bar: 100 μm; inset 50 μm. (**I**) Schematic of 3D-printed scaffold structure. (**J**) Stereomicroscope image of scaffold lattice structure of 10% μtank scaffold; Scale bar: 2 mm. (**K**) Average pore area for scaffolds of varying μtank concentrations (n = 6–10). Red dashed line: theoretical pore area. (**L**) Average strut thickness for scaffolds of varying μtank concentrations (n = 6–10). Red dashed line: theoretical strut thickness.

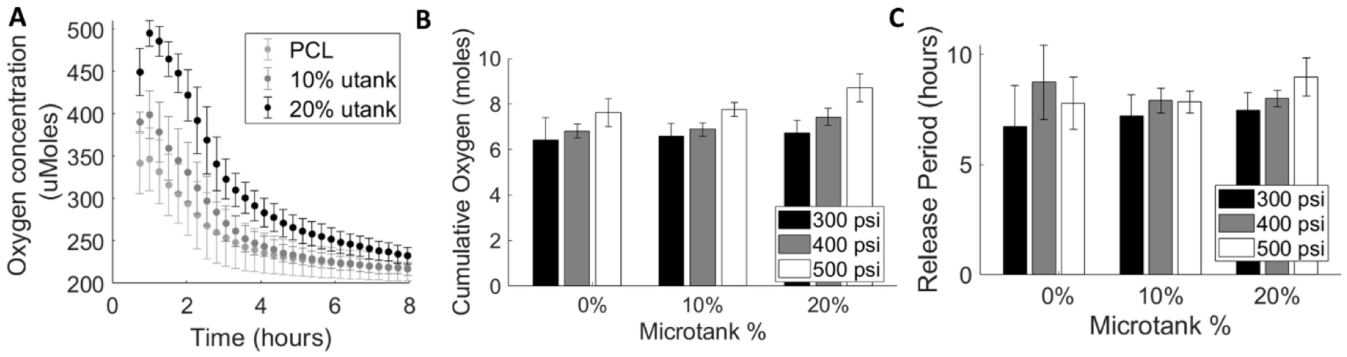

Figure 2: O_2 release can be tuned by changing µtank concentration and loading pressure.

(**A**) O_2 release was measured from 0%, 10%, and 20% µtank-PCL scaffolds hyperbarically loaded at 300, 400, and 500 psi for 1 week (n = 5). (**B**) Cumulative release amounts were determined by integrating the release curves over the time of measurement. (**C**) The release periods were calculated by fitting an exponential curve $\left(y = a * e^{-\lambda t}\right)$ to the release curves, finding the time constants of release (λ), and using the time constants to calculate the amount of time it takes for O_2 to equilibrate (reach 192 µM).

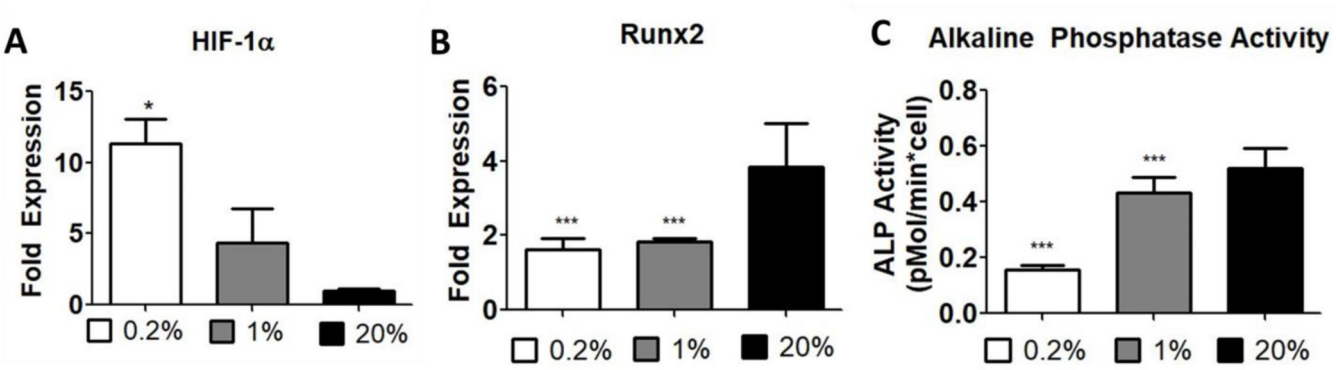

Figure 3: Hypoxia inhibits the expression of early stage osteogenic markers in ASCs

Passage 2 ASCs cultured in osteogenic media for 7 days in 0.2%, 1%, or 20% O_2 (n = 4–6; *, **, *** represent $p < 0.05$, 0.01, 0.001). Gene expression of **(A)** HIF-1α and **(B)** Runx2. **(C)** Alkaline phosphatase activity of ASC lysates.

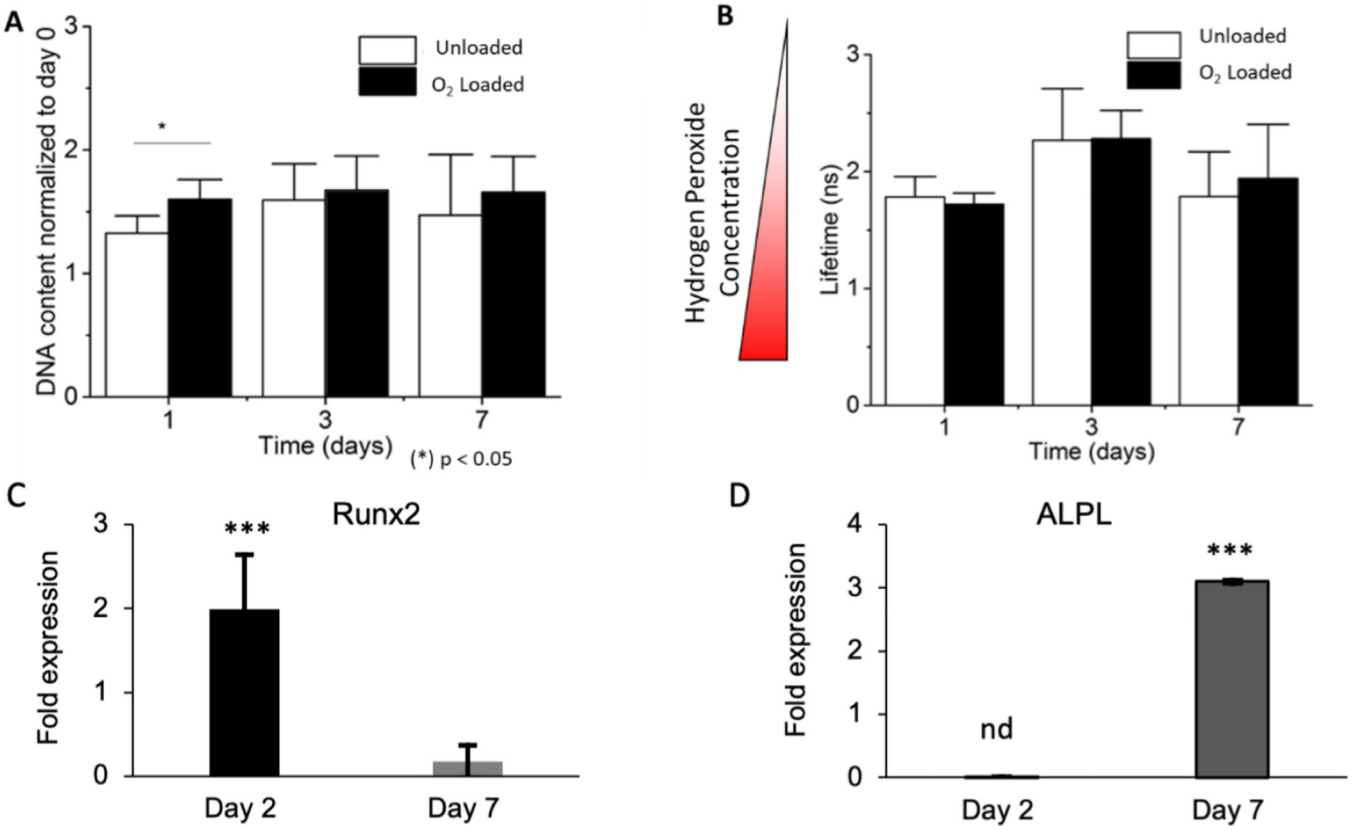

Figure 4: µtank-mediated O_2 delivery does not increase long term DNA content or oxidative stress, however impacts early-stage osteogenic markers.

(**A**) DNA content of ASCs encapsulated in fibrin within the pore spaces of Unloaded or O_2-Loaded 10% µtank scaffolds (n = 4–6). (**B**) Intracellular hydrogen peroxide concentration of ASCs measured by fluorescent lifetime imaging using a HyPer3 sensor (n = 15). (C) Runx2 fold expression of ASCs in presence of O2 loaded 20% µtank scaffolds at day 2 and day 7 of culture normalized to GAPDH and unloaded µtank scaffolds (n= 6). (**D**) ALPL expression of ASCs in presence of O2 loaded 20% µtank scaffolds at day 2 and day 7 of culture normalized to GAPDH and unloaded µtank scaffolds (n= 6). (n = 4–6; *, **, *** represent $p < 0.05$, 0.01, 0.001, nd= undetermined).

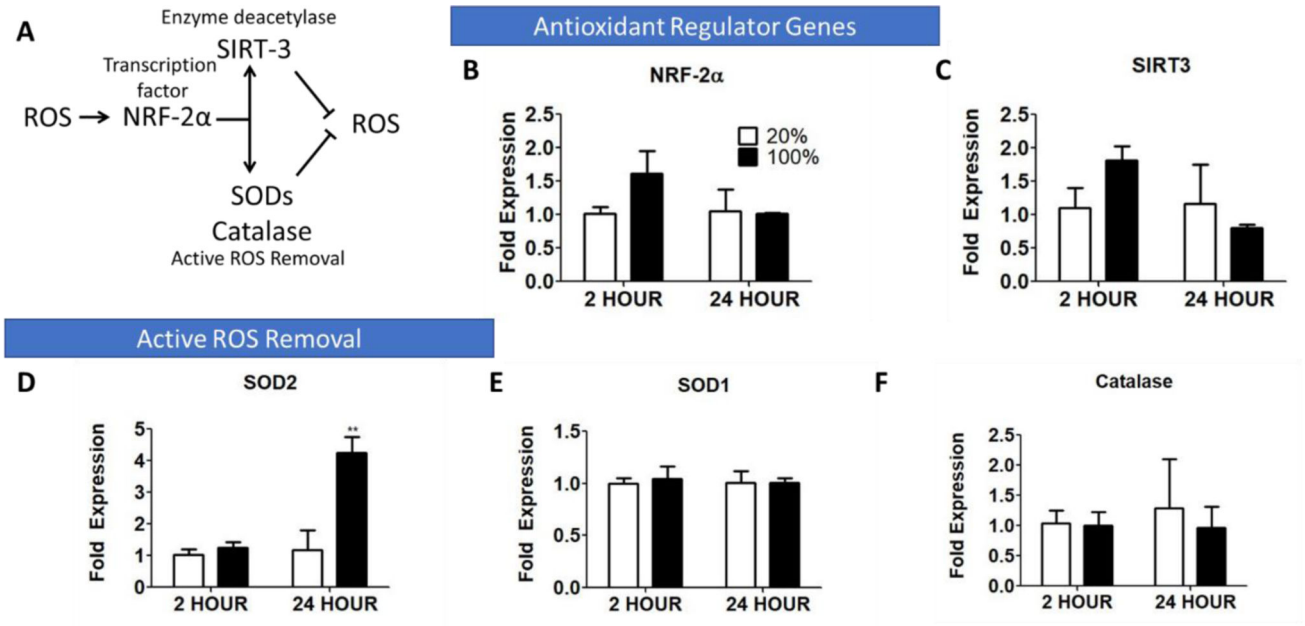

Figure 5: ASCs exposed to hyperoxia (100% O_2) for a short-term (24 hours) upregulate intrinsic antioxidant pathways to compensate for increased O_2 tension.

(**A**) Schematic of antioxidant regulatory gene pathways. Comparison of the expression of: (**B**) NRF-2α, (**C**) SIRT3, and ROS-neutralizing enzymes (**D**) SOD2, (**E**) SOD1, and (**F**) Catalase. (n = 4–6; *, **, *** represent $p < 0.05, 0.01, 0.001$).

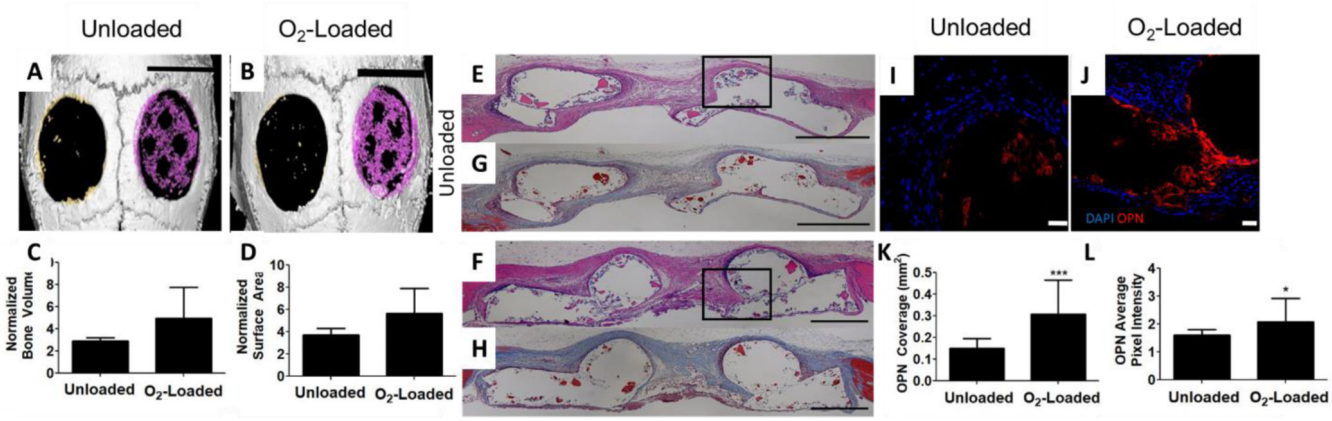

Figure 6: O_2 delivery from µtank scaffolds increases matrix and osteogenic protein deposition.

Unloaded or O_2-loaded 20% µtank scaffolds and ASCs were implanted into 4 mm murine calvarial defects for 8 weeks. (**A**, **B**) µCT of calvarial defects with scaffolds pseudocolored magenta and compared to empty defects in the contralateral side; scale bar = 4 mm. (**C**) Quantification of bone volume normalized to empty defect (n = 5), (**D**) Quantification of bone cross-sectional area compared to empty defect (n = 5), (**E**,**F**) H&E (inset boxes show where OPN immunostaining in I and J were taken from) and (**G**, **H**) Masson's trichrome staining; Scale bar in E-H = 500 µm, (**I**, **J**) Immunofluorescence images of osteopontin staining; Scale bar = 50 µm, (**K**) Quantification of OPN immunostained area (n = 12), (**L**) Quantification of OPN signal intensity (n = 12). (*,*** represent $p < 0.05, 0.001$).

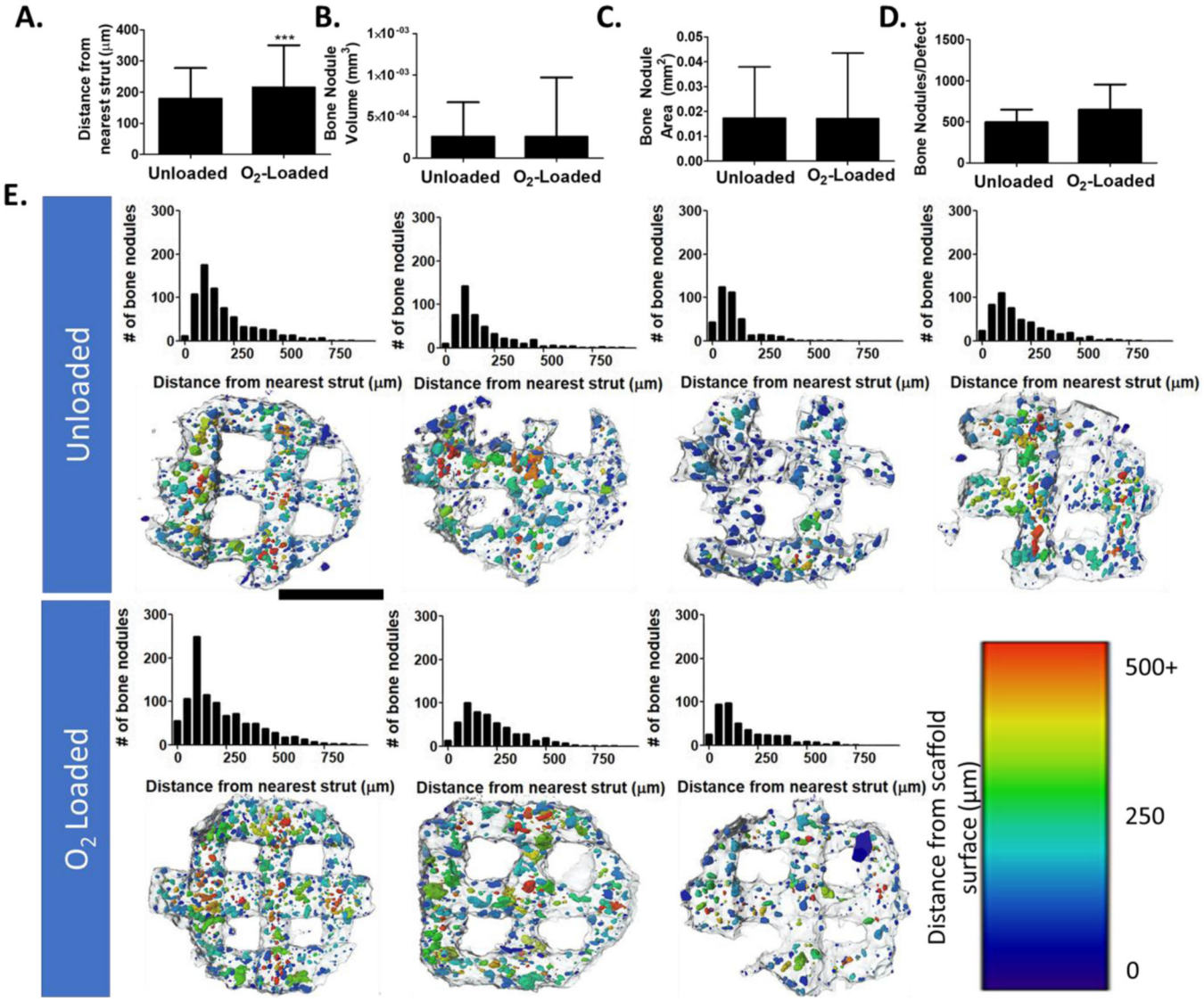

Figure 7: Analysis of bone particle distribution in calvarial defects.

(**A**) Average distance between the center of mass of each bone nodule and its nearest scaffold surface. (**B**) Average volume of bone nodules. (**C**) Average surface area of bone nodules. (**D**) Average number of bony nodules in each defect. (**E**, top) Histograms of each analyzed sample representing distance of bone nodules from the nearest scaffold surface. (**E**, bottom) CT data with scaffolds outlined in gray and bone nodules pseudocolored based on distance from the surface. (n = 4, 3; *** represent $p < 0.001$). Scale bar = 2 mm.

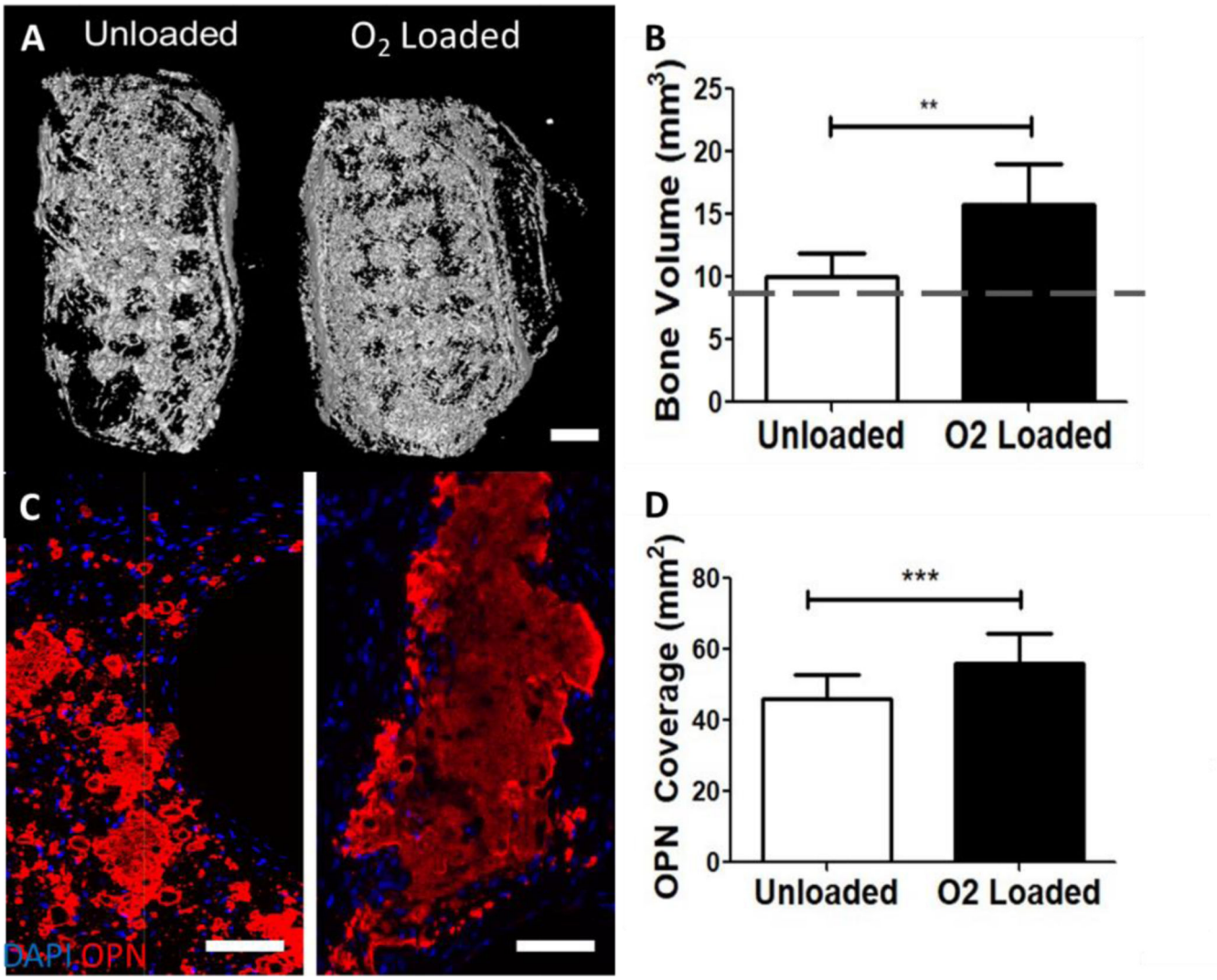

Figure 8: O_2 delivery from µtank scaffolds increases mineralization and osteogenic protein deposition in ectopic defects.

Unloaded or O_2-loaded 10% µtank scaffolds and ASCs were implanted into dorsal subcutaneous defects for 8 weeks. (**A**) CT of calvarial defects; Scale bar = 1 mm. (**B**) Quantification of bone area compared to empty defect; dashed line is average initial scaffold bone volume (n = 8). (**C**) Immunofluorescence images of osteopontin staining; scale bar = 100 µm. (**D**) Quantification of OPN immunostained area within the defects (n = 16–22). **, *** represent $p < 0.01, 0.001$).

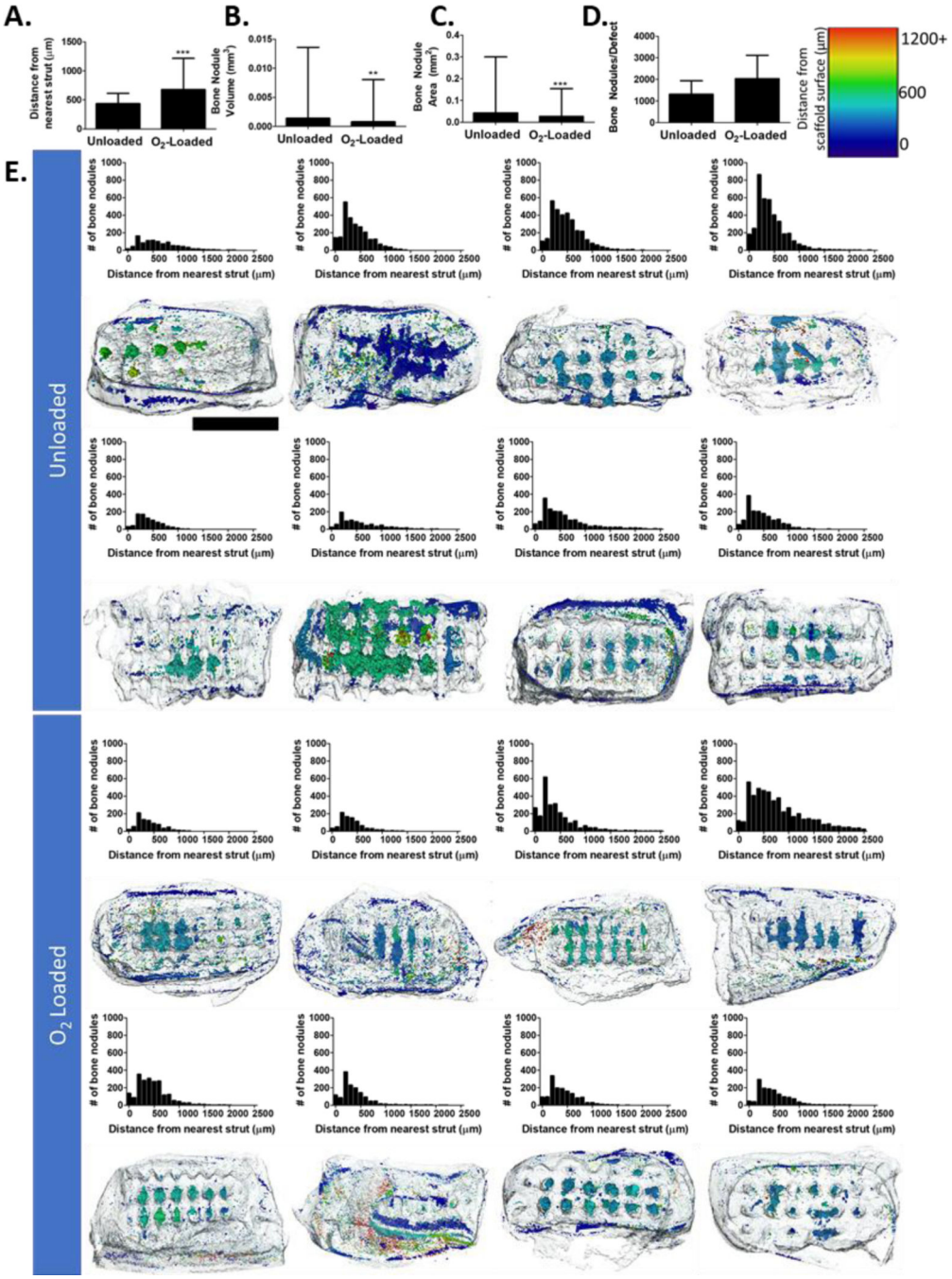

Figure 9: Analysis of bone particle distribution in subcutaneous defects.

(**A**) Average distance between the center of mass of each bone nodule and its nearest scaffold surface. **(B**) Average volume of bone nodules. (**C**) Average surface area of bone nodules. (**D**) Average number of bony nodules in each defect. (**E**, top) Histograms of each analyzed sample representing distance of bone nodules from the nearest scaffold surface. (**E**, bottom) CT data with scaffolds outlined in gray and bone nodules pseudocolored based on their distance from the surface. (n = 8; **, *** represent $p < 0.01$, 0.001). Scale bar = 4 mm.